Journal of Glaciology



Article

Cite this article: Stubblefield AG, Meyer CR, Siegfried MR, Sauthoff W, Spiegelman M (2023). Reconstructing subglacial lake activity with an altimetry-based inverse method. *Journal of Glaciology* **69**(278), 2139–2153. https://doi.org/10.1017/jog.2023.90

Received: 27 April 2023
Revised: 4 October 2023
Accepted: 11 October 2023
First published online: 8 November 2023

Keywords:
Antarctic glaciology; ice-sheet modeling; subglacial lakes; subglacial processes

Corresponding author:
Aaron Stubblefield;
Email: aaron.g.stubblefield@dartmouth.edu

© The Author(s), 2023. Published by Cambridge University Press on behalf of International Glaciological Society. This is an Open Access article, distributed under the terms of the Creative Commons Attribution licence (http://creativecommons.org/licenses/by/4.0/), which permits unrestricted re-use, distribution and reproduction, provided the original article is properly cited.

cambridge.org/jog

Reconstructing subglacial lake activity with an altimetry-based inverse method

Aaron G. Stubblefield[1], Colin R. Meyer[1], Matthew R. Siegfried[2,3], Wilson Sauthoff[3] and Marc Spiegelman[4,5]

[1]Thayer School of Engineering, Dartmouth College, Hanover, NH, USA; [2]Department of Geophysics, Colorado School of Mines, Golden, CO, USA; [3]Hydrologic Science and Engineering Program, Colorado School of Mines, Golden, CO, USA; [4]Lamont-Doherty Earth Observatory, Columbia University, Palisades, NY, USA and [5]Department of Applied Physics and Applied Mathematics, Columbia University, New York, NY, USA

Abstract

Subglacial lake water-volume changes produce ice-elevation anomalies that provide clues about water flow beneath glaciers and ice sheets. Significant challenges remain in the quantitative interpretation of these elevation-change anomalies because the surface expression of subglacial lake activity depends on basal conditions, rate of water-volume change, and ice rheology. To address these challenges, we introduce an inverse method that reconstructs subglacial lake activity from altimetry data while accounting for the effects of viscous ice flow. We use a linearized approximation of a Stokes ice-flow model under the assumption that subglacial lake activity only induces small perturbations relative to a reference ice-flow state. We validate this assumption by accurately reconstructing lake activity from synthetic data that are produced with a fully nonlinear model. We then apply the method to estimate the water-volume changes of several active subglacial lakes in Antarctica by inverting data from NASA's Ice, Cloud, and land Elevation Satellite 2 (ICESat-2) laser altimetry mission. The results show that there can be substantial discrepancies (20% or more) between the inversion and traditional estimation methods due to the effects of viscous ice flow. The inverse method will help refine estimates of subglacial water transport and further constrain the role of subglacial hydrology in ice-sheet evolution.

1. Introduction

Ice-sheet surface elevation responds to a variety of time-varying subglacial phenomena, including subglacial-lake volume change, basal-drag variations, and melting or freezing at the ice-water interface. Active subglacial lakes (i.e., those that experience observable volume change in the observational record) in particular have received much attention due to the localized perturbations they produce in ice-sheet surface elevation during volume-change events (e.g., Gray and others, 2005; Wingham and others, 2006; Fricker and others, 2007). NASA's Ice, Cloud, and land Elevation Satellite (ICESat) mission (2003-2009) and the European Space Agency's CryoSat-2 satellite altimetry mission (2010-present) facilitated the detection of over one hundred active subglacial lakes beneath the Antarctic Ice Sheet (e.g., Smith and others, 2009; Wright and Siegert, 2012; Fricker and others, 2016; Livingstone and others, 2022), driving investigations into their possible relation to fast ice flow (e.g., Stearns and others, 2008; Scambos and others, 2011; Siegfried and others, 2016) and into their ability to host microbial ecosystems (e.g., Christner and others, 2014; Achberger and others, 2016; Davis and others, 2023). Fewer subglacial lakes have been discovered beneath the Greenland Ice Sheet based on ice-surface changes, suggesting that there may be significant differences in subglacial hydrological conditions there relative to the Antarctic Ice Sheet (e.g., Bowling and others, 2019; Livingstone and others, 2019, 2022).

High-resolution satellite altimetry data from NASA's ICESat-2 mission (2018-present) presents a valuable opportunity to continue investigating dynamic conditions and constraining water budgets beneath ice sheets (e.g., Markus and others, 2017; Neckel and others, 2021; Siegfried and Fricker, 2021). ICESat-2's temporal resolution (91 day repeat cycle) and spatial resolution (~3.3 km across-track between beam pairs and ~90 m between beams within the pairs) provide unprecedented coverage of active subglacial lakes, which are typically greater than ~10 km in diameter and fill or drain over multiple years (Smith and others, 2009; Siegfried and Fricker, 2021; Stubblefield and others, 2021a). Modeling has shown that accurately estimating subglacial-lake volume change, areal extent, and highstand or lowstand timing from altimetry alone can be complicated by the effects of viscous ice flow (Stubblefield and others, 2021a). Basal vertical velocity anomalies associated with subglacial lake activity can manifest with a wider areal extent and smaller amplitude at the ice-sheet surface when ice flows laterally toward or away from the lake during volume-change events. Ice viscosity, ice thickness, and basal drag exert strong control on ice flow and, therefore, also influence the surface expression of subglacial lake activity (Stubblefield and others, 2021a). Although satellite altimetry data has been incorporated in basal-drag inversions (e.g., Larour and others, 2014; Arthern and others, 2015; Goldberg and others, 2015; Mosbeux and others, 2016), inverse methods that quantify subglacial-lake activity from altimetry and account for ice-flow effects have not yet been developed.

Inversion of time-varying altimetry data necessitates leveraging reduced-order models to alleviate the computational cost associated with repeatedly solving the forward problem. Dimensionality reduction is often achieved using ice-flow models that are based on depth-integrated approximations of the Stokes equations (e.g., Greve and Blatter, 2009). Solving the linearized Stokes equations on simplified domains with spectral methods is an alternative way to achieve computational efficiency when the full stresses in the ice must be resolved (e.g., Budd, 1970; Hutter and others, 1981; Balise and Raymond, 1985; Gudmundsson, 2003; Sergienko, 2012). Previous inversions relying on perturbation methods have not included time-varying data (Gudmundsson and Raymond, 2008; Thorsteinsson and others, 2003). Likewise, a computational method for inverting time-varying elevation data with perturbation-based models would be a valuable step toward quantifying time-varying subglacial lake perturbations. We use this small-perturbation approach as subglacial lake activity typically only induces small perturbations in ice-surface elevation (e.g., a few meters) relative to ice thickness.

Here, we derive, test, and apply an altimetry-based inverse method for quantifying basal vertical velocity perturbations that arise from subglacial lake activity. First, we outline the forward model for the perturbation in ice-surface elevation that is produced by a basal vertical velocity forcing. We then derive the inverse method from a least-squares optimization problem. To verify and validate the method, we present tests with synthetic data from both the linearized and nonlinear models. We then apply the method to a collection of active subglacial lakes in Antarctica (Fig. 1). The results show that ice flow can produce significant discrepancies between the inverse method and a traditional altimetry-based estimation method for calculating changes in subglacial water volume over the current ICESat-2 time period. We conclude by discussing limitations, extensions, and further applications of the method.

2. Method

In this section, we derive the forward model and the associated inverse method. First, we outline the general Stokes flow problem to highlight the governing equations and simplifying assumptions. Then, we outline a derivation of the small-perturbation

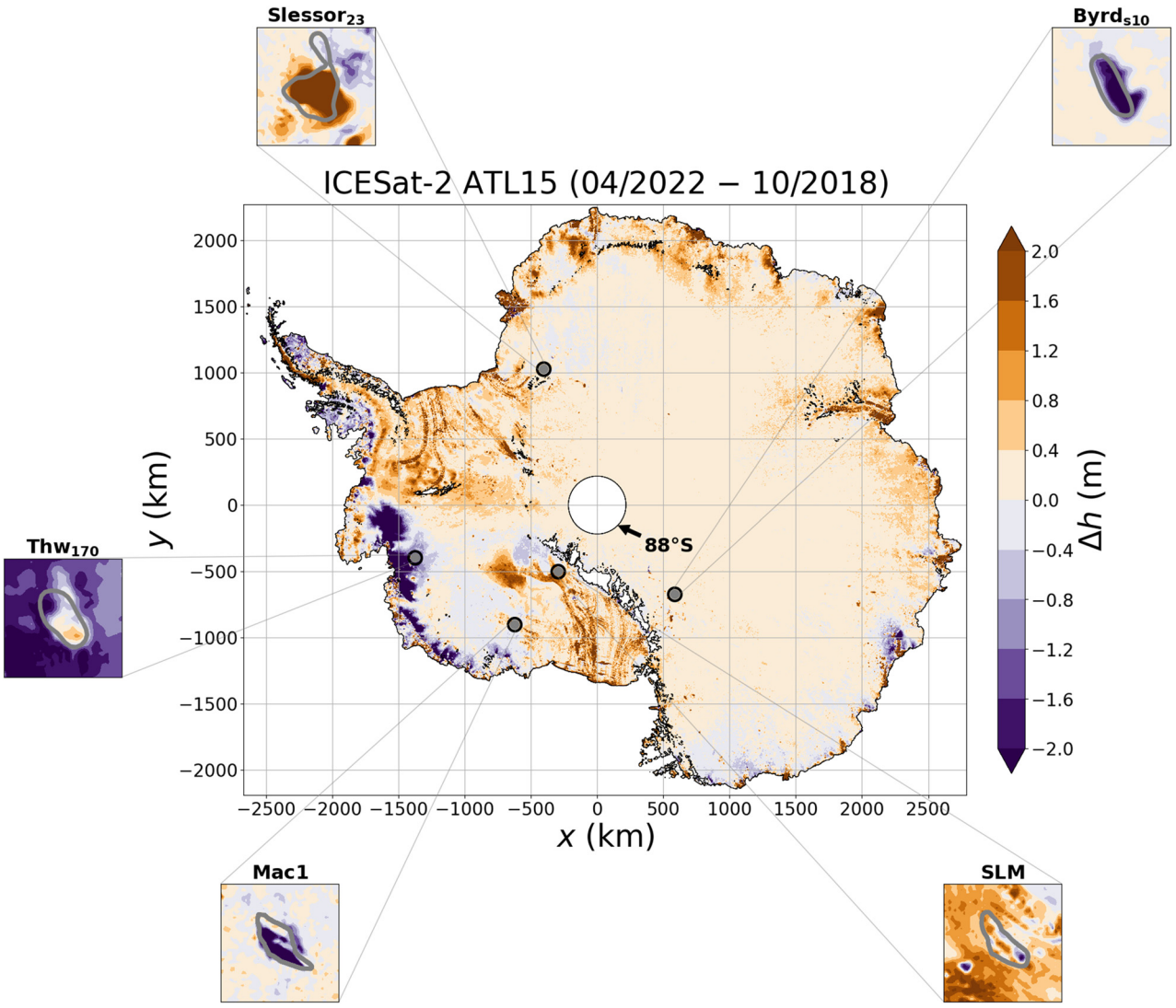


Figure 1. Map of ICESat-2 ATL15 gridded product (Smith and others, 2022) showing the elevation change of the Antarctic Ice Sheet between October 2018 and April 2022. The map-plane (x, y) coordinates in the ATL15 dataset correspond to the Antarctic Polar Stereographic Projection (EPSG:3031). Insets show the locations of the subglacial lakes targeted as examples in this study. Subglacial lake boundaries derived from surface altimetry are shown as gray lines (Siegfried and Fricker, 2018). Regional thinning occurs around Thwaites Lake 170 (Thw_{170}) and regional thickening occurs around Mercer Subglacial Lake (SLM). Regional elevation-change trends around Slessor Glacier (lake Slessor_{23}), MacAyeal Ice Stream (lake Mac1), and Byrd Glacier (lake Byrd_{s10}) are less pronounced. We remove regional trends to produce elevation-change anomalies that are used in the inversions.

https://doi.org/10.1017/jog.2023.90 Published online by Cambridge University Press

model that is used in the inverse method. Finally, we derive the inverse method with a least-squares optimization approach.

2.1. Stokes flow

We assume that ice deforms as a viscous fluid according to the incompressible Stokes equations, which are given by

$$-\nabla\cdot\boldsymbol{\sigma}=\rho_{\mathrm{i}}\boldsymbol{g}, \tag{1}$$

$$\nabla\cdot\boldsymbol{u}=0, \tag{2}$$

where ρ_{i} is the ice density, $\boldsymbol{u}=[u,\ v,\ w]^{\mathrm{T}}$ is the ice velocity, and $\boldsymbol{g}=g[0,\ 0,\ -1]^{\mathrm{T}}$ denotes gravitational acceleration with magnitude $g=9.81\ \mathrm{m\,s^{-2}}$ (Greve and Blatter, 2009; Stubblefield and others, 2021b). We have excluded possible elastic components of ice deformation by assuming a viscous rheology and revisit this choice in the discussion. The stress tensor $\boldsymbol{\sigma}$ is defined via

$$\boldsymbol{\sigma}=-pI+\eta\left(\nabla\boldsymbol{u}+\nabla\boldsymbol{u}^{\mathrm{T}}\right), \tag{3}$$

where p is the pressure, I is the identity tensor, and η is the viscosity. At the ice-bed boundary we assume a sliding law of the form

$$T\boldsymbol{\sigma}\boldsymbol{n}=-\beta T\boldsymbol{u}, \tag{4}$$

where β is the basal drag coefficient, $\boldsymbol{n}$ is an outward-pointing unit normal to the boundary, and $T=I-\boldsymbol{n}\boldsymbol{n}^{\mathrm{T}}$ is a projection tangential to the ice-sheet surface (Stubblefield and others, 2021b). Although the small-perturbation model used in the inversions assumes a Newtonian viscosity and linear sliding law (i.e., constant η and β), we will also consider synthetic data produced by a fully nonlinear model with Glen's law viscosity (Glen, 1955) and a nonlinear Weertman-style sliding law (Weertman, 1957) to test the validity of these simplifications.

The upper surface of the ice-sheet $z=h(x,\ y,\ t)$ evolves over time according to the kinematic equation

$$\frac{\partial h}{\partial t}+u\frac{\partial h}{\partial x}+v\frac{\partial h}{\partial y}=w, \tag{5}$$

where the velocity components are evaluated at the surface ($z=h$). We assume that a stress-free condition,

$$\boldsymbol{\sigma}\boldsymbol{n}=\boldsymbol{0}, \tag{6}$$

holds at the upper surface of the ice sheet. We approximate the spatial domain as a horizontally unbounded slab because the ice-sheet extent is much greater than areal extent of the subglacial lakes. Away from the lake, we assume that all quantities approach an appropriate far-field reference state that is based on data and available ice-sheet model output.

2.2. Small-perturbation model

Now we will describe the forward model that is used in the inverse method. Although small-perturbation models have been derived previously, we outline a derivation here to highlight the assumptions underlying the inverse method (Balise and Raymond, 1985; Gudmundsson, 2003). Our goal is to find the basal vertical velocity perturbation w_{b} that produces the surface elevation-change anomaly Δh_{a} under the assumption that these anomalies arise from subglacial lake activity (Fig. 2). We could also incorporate a basal drag anomaly to represent a slippery spot over a lake in the small-perturbation framework (e.g., Gudmundsson, 2003; Stubblefield, 2022), but the resulting dipolar elevation-change anomaly (Sergienko and others, 2007) is not discernible in any of the active lakes considered herein. We revisit this idea in the discussion.

To derive a simplified model for this system, we assume that Δh_{a} and w_{b} are small perturbations from a known reference state that is (approximately) characterized by a constant ice thickness $\bar{H}$, horizontal surface velocity $\bar{\boldsymbol{u}}=[\bar{u},\ \bar{v}]^{T}$, ice viscosity $\bar{\eta}$, and basal drag coefficient $\bar{\beta}$. We further assume that the basal surface is horizontal in the reference state and that the ice pressure equals the cryostatic pressure. Strictly speaking, an advective component is only present in the free-slip limit ($\bar{\beta}=0$) under the assumption of a horizontally uniform Stokes flow over a flat bed subject to the stress boundary conditions (4) and (6). However, we retain a background advective velocity in all cases for consistency with the data.

Letting $[u_h,\ v_h,\ w_h]^{T}$ denote the perturbation in ice-sheet surface velocity, we insert perturbations to the reference states, $h=\bar{H}+\Delta h_{\mathrm{a}}$ and $\boldsymbol{u}=[\bar{u},\ \bar{v},\ 0]^{T}+[u_h,\ v_h,\ w_h]^{T}$, into the kinematic equation (5) to obtain

$$\frac{\partial\Delta h_{\mathrm{a}}}{\partial t}+\bar{u}\frac{\partial\Delta h_{\mathrm{a}}}{\partial x}+\bar{v}\frac{\partial\Delta h_{\mathrm{a}}}{\partial y}=w_h. \tag{7}$$

We have neglected terms involving products of perturbations in (7) under the assumption of small perturbations. We solve equation (7) by taking Fourier transforms with respect to the horizontal coordinates $(x,\ y)$ to obtain

$$\frac{\partial\widehat{\Delta h_{\mathrm{a}}}}{\partial t}+(i\boldsymbol{k}\cdot\bar{\boldsymbol{u}})\widehat{\Delta h_{\mathrm{a}}}=\widehat{w_h}, \tag{8}$$

where $\boldsymbol{k}=[k_x,\ k_y]^{\mathrm{T}}$ is the horizontal wavevector. The vertical surface velocity is assumed to satisfy the Stokes flow problem (1)–(6), subject to the above simplifications, which allows us to derive a closed-form expression of the solution operator (Balise and

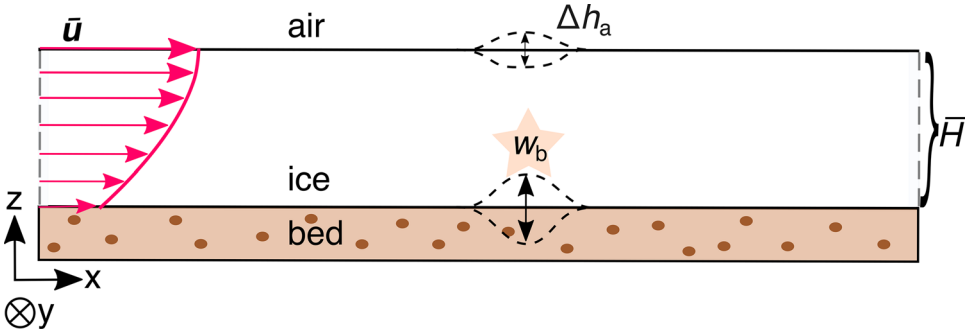


Figure 2. Sketch of linearized model setup. The horizontal (map-plane) coordinates are $(x,\ y)$ with the y direction pointing into the page. The basal vertical velocity anomaly w_{b} produces an elevation-change anomaly Δh_{a}. The ice thickness is $\bar{H}$ and the horizontal surface velocity is $\bar{u}$ in the reference flow state. The ice flow is aligned with the x axis here for simplicity but generally also has a component in the y direction. The volume change estimated from the elevation-change anomaly Δh_{a} can deviate significantly from the subglacial water-volume change (Stubblefield and others, 2021a).

https://doi.org/10.1017/jog.2023.90 Published online by Cambridge University Press

Raymond, 1985; Gudmundsson, 2003; Stubblefield and others, 2021a).

We algebraically solve the Fourier-transformed Stokes problem to obtain an expression for the transformed vertical surface velocity,

$$\widehat{w_h} = -\mathcal{R}\widehat{\Delta h_a} + \mathcal{T}\widehat{w_b}, \tag{9}$$

in terms of the basal vertical velocity and surface elevation anomalies (e.g., Stubblefield and others, 2021a, Supporting Information). In Eqn. (9), $\mathcal{R}$ is a relaxation function that controls the decay rate of the elevation anomaly, and $\mathcal{T}$ is a transfer function that maps the basal vertical velocity anomaly to its surface expression. These functions depend on the scaled wavevector magnitude $k' = |\boldsymbol{k}|\bar{H}$ and drag coefficient $\gamma = \bar{\beta}\bar{H}/(2\bar{\eta}k')$ through the relations

$$\mathcal{R} = \left(\frac{\rho_i g\bar{H}}{2\bar{\eta}k'}\right) \times \frac{(1+\gamma)e^{4k'} - (2+4\gamma k')e^{2k'} + 1 - \gamma}{(1+\gamma)e^{4k'} + (2\gamma + 4k' + 4\gamma k'^2)e^{2k'} - 1 + \gamma}, \tag{10}$$

and

$$\mathcal{T} = \frac{2(1+\gamma)(k'+1)e^{3k'} + 2(1-\gamma)(k'-1)e^{k'}}{(1+\gamma)e^{4k'} + (2\gamma + 4k' + 4\gamma k'^2)e^{2k'} - 1 + \gamma}. \tag{11}$$

For a detailed derivation of the expressions (10) and (11) see, for example, Stubblefield and others (2021a, Supporting Information) and Stubblefield (2022, Appendix E).

Substituting the expression (9) into (8), we find that the ice-surface elevation anomaly Δh_a evolves in frequency space via

$$\frac{\partial\widehat{\Delta h_a}}{\partial t} + (i\boldsymbol{k}\cdot\bar{\boldsymbol{u}})\widehat{\Delta h_a} = -\mathcal{R}\widehat{\Delta h_a} + \mathcal{T}\widehat{w_b}. \tag{12}$$

The solution to equation (12) is given by

$$\widehat{\Delta h_a} = \widehat{\Delta h_0}e^{-(i\boldsymbol{k}\cdot\bar{\boldsymbol{u}}+\mathcal{R})t} + \widehat{w_b} * \mathcal{K}, \tag{13}$$

where * denotes convolution over time and Δh_0 is the elevation perturbation at the initial time $t = 0$. The kernel $\mathcal{K}$, defined by

$$\mathcal{K} = \mathcal{T}e^{-(i\boldsymbol{k}\cdot\bar{\boldsymbol{u}}+\mathcal{R})t}, \tag{14}$$

controls the decay of the elevation-change anomaly and transfer of the basal anomaly to the surface. The characteristic time scale for the decay of surface-elevation anomalies is

$$t_{\text{relax}} = \frac{2\bar{\eta}}{\rho_i g\bar{H}}, \tag{15}$$

which controls the magnitude of the relaxation function $\mathcal{R}$ (cf. Turcotte and Schubert, 2014, Chapter 6). The effects of viscous ice flow influence the surface expression of lake activity when the viscous relaxation time t_{relax} is comparable to the lake filling or draining timescale (Stubblefield and others, 2021a). We highlight the importance of the viscous relaxation time in the examples below.

2.3. Inverse method

Now we will outline the inverse method. We let F denote the (map-plane) Fourier transform operator and define the relative elevation-change anomaly via

$$d = \Delta h_a - F^{-1}\left(e^{-(i\boldsymbol{k}\cdot\bar{\boldsymbol{u}}+\mathcal{R})t}F(\Delta h_0)\right), \tag{16}$$

which has the contribution from the initial value in equation (13) removed. From equation (13), we define the operator G that maps w_b to the relative elevation change d via

$$G(w_b) = F^{-1}(F(w_b) * \mathcal{K}), \tag{17}$$

where the kernel $\mathcal{K}$ is defined in equation (14).

We consider a regularized least-squares objective functional,

$$J(w_b) = \frac{1}{2}\int_0^{t_f}\int_{-\infty}^{+\infty}\int_{-\infty}^{+\infty} |G(w_b) - d|^2 \,\mathrm{d}x\,\mathrm{d}y\,\mathrm{d}t + \frac{\varepsilon}{2}\int_0^{t_f}\int_{-\infty}^{+\infty}\int_{-\infty}^{+\infty} |\nabla w_b|^2 \,\mathrm{d}x\,\mathrm{d}y\,\mathrm{d}t, \tag{18}$$

where t_f is the final time and the parameter ε controls the strength of the regularization term. While the regularization in (18) promotes smoothness, other regularizations could be chosen to promote sparsity of the basal forcing, for example (Stadler, 2009). The minimizer of the objective (18) satisfies the normal equation

$$G^*(G(w_b)) - \varepsilon\nabla^2 w_b = G^*(d), \tag{19}$$

which can be derived with variational calculus (Vogel, 2002; Hanke, 2017). The adjoint operator G^* in (19) is given by

$$G^*(f) = F^{-1}(F(f) \bigstar \mathcal{K}) \tag{20}$$

for any function f, where ★ denotes cross-correlation over time.

We solve the equation (19) with the conjugate gradient method to obtain the basal vertical velocity w_b. In using the conjugate gradient method to solve this operator equation, we avoid explicitly constructing matrices corresponding to the forward and adjoint operators, and instead simply require the action of these operators on functions (Atkinson and Han, 2009, Section 5.6). We implemented the discretized inverse method in Python with SciPy's fast Fourier transform and convolution algorithms (Virtanen and others, 2014). The code is openly available (https://doi.org/10.5281/zenodo.8371416).

2.4. Estimation of water-volume change

To compare the inversion with previous estimation methods, we will focus on estimating subglacial water-volume changes. Given the basal vertical velocity inversion w_b, the basal water-volume change over a map-plane area B can be computed via

$$\Delta V_{\text{inv}}(t) = \int_0^t \left[\iint_B w_b \,\mathrm{d}x\,\mathrm{d}y\right]\mathrm{d}t'. \tag{21}$$

Alternatively, the volume-change has often been estimated in previous studies by integrating the elevation change anomaly over the static outline of a lake (Fricker and Scambos, 2009; Smith and others, 2009). Using this approach, the water-volume change is estimated by

$$\Delta V_{\text{alt}}(t) = \iint_B \Delta h_a - \Delta h_0 \,\mathrm{d}x\,\mathrm{d}y, \tag{22}$$

https://doi.org/10.1017/jog.2023.90 Published online by Cambridge University Press

where we have integrated over the same map-plane area B. Although an alternative lake boundary could be identified with the inversion, we use the same boundary to calculate both estimates for consistency in comparison. We revisit this problem in the discussion.

In the limits $\mathcal{R} \to 0$ and $\mathcal{T} \to 1$, equation (12) implies that these volume changes are equivalent (i.e., $\Delta V_{\text{inv}} = \Delta V_{\text{alt}}$). This "rigid-ice" limit is approached when the ice is viscous enough for the relaxation timescale, t_{relax} (eq. (15)), to greatly exceed the volume-change timescale (Stubblefield and others, 2021a). Although incompressibility causes these volume changes to be equal when integrating over the entire areal extent of a glacier, this approach is impractical for the Antarctic Ice Sheet due to the presence of multiple lakes and regional thickening or thinning trends. We explore the discrepancy between the inversion-derived estimate (21) and surface-derived estimate (22) for a range of parameters in the examples below.

3. Synthetic examples

Before applying the method to the ICESat-2 altimetry data, we first solve two problems with synthetic data to validate the method and illustrate the range of behaviors found in the ICESat-2 examples below. First, we verify the implementation by inverting synthetic data that is produced by prescribing the linearized model with a known basal vertical velocity field and then adding Gaussian white noise to the resulting elevation change. For consistency with the ICESat-2 examples, we remove a small off-lake elevation-change component, Δh_{off}, from the elevation change as detailed in the next section. For this example, we choose a basal vertical velocity field that is a Gaussian bump undergoing sinusoidal oscillations in time. The inverse method is able to reconstruct the basal vertical velocity and volume-change time series from the synthetic data (Fig. 3). We find that there is little deviation ($\lesssim 5\%$) between the volume-change estimates (21) and (22) on short timescales (i.e., less than ~2.5

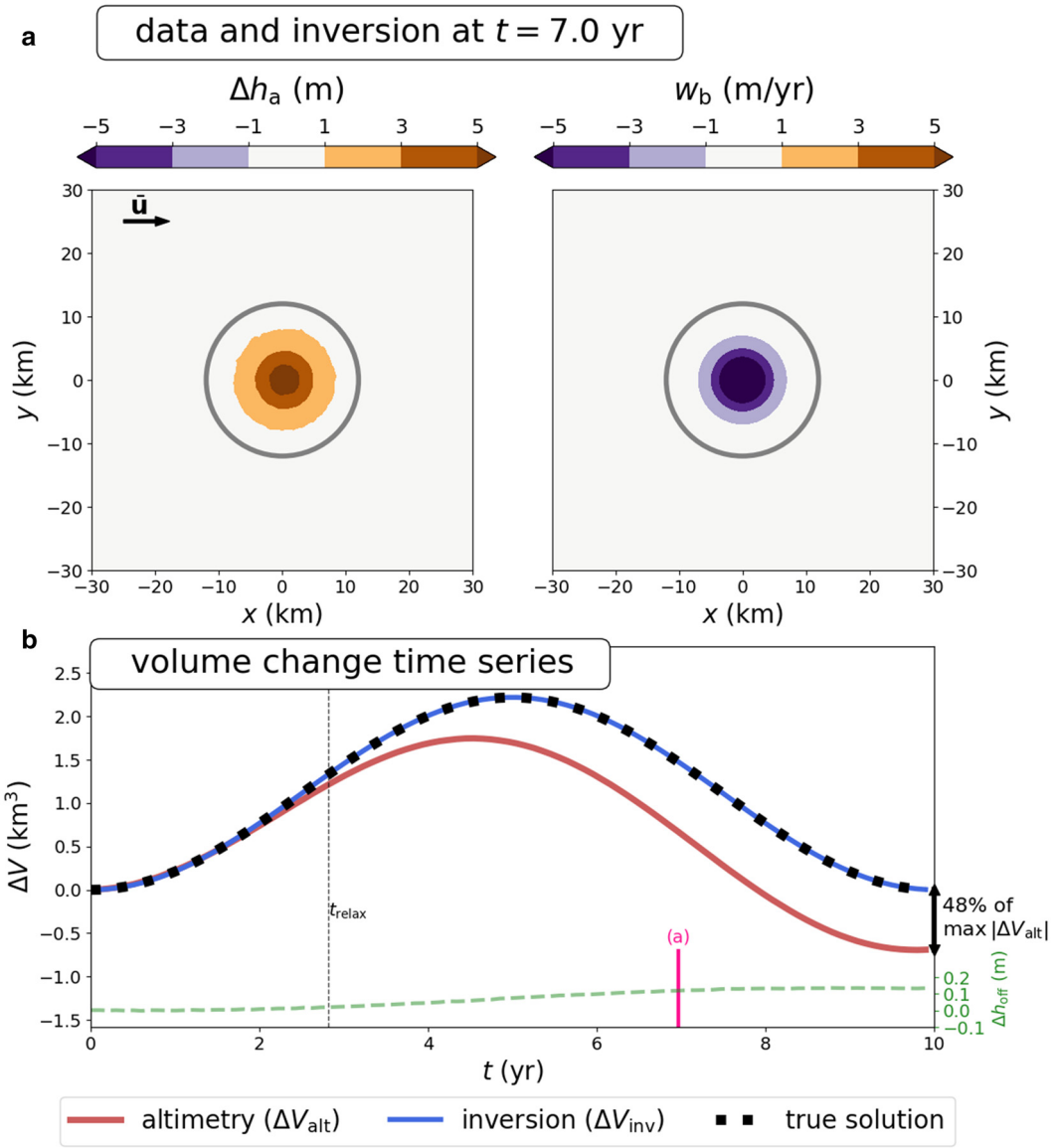


Figure 3. Inversion results for synthetic data produced with the linearized model. (a) Map-plane elevation anomaly and inversion at $t = 7$ yr. (b) Time series of the surface-derived volume change (ΔV_{alt}), the inversion-based volume change (ΔV_{inv}), and the off-lake component (Δh_{off}) that is removed prior to inversion. The gray contours in (a) and (b) show the boundaries used to compute the volume-change time series. The ice flow direction is shown by the black arrow in (a). The maximum deviation between the surface-derived volume change and the inversion in (b) is 0.83 km^3, or 48% of the maximum amplitude of the surface-derived estimate. The inversion accurately recovers the true water-volume change (dashed black line). The parameters for this example are $\bar{H} = 2500$ m, $\bar{\eta} = 10^{15}$ Pa s, $\bar{\beta} = 10^{11}$ Pa s m^{-1}, $\bar{u} = 200$ m yr^{-1}, and $\bar{v} = 0$ m yr^{-1}. The viscous relaxation time associated with these parameters is $t_{\text{relax}} = 2.82$ yr. The pink line marks the time step shown in (a). See Movie S1 for an animation of the inversion over all time steps.

https://doi.org/10.1017/jog.2023.90 Published online by Cambridge University Press

years), whereas large deviations occur over decadal timescales. This behavior arises because the viscosity is $\bar{\eta} = 10^{15}$ Pa s for this example, leading to characteristic relaxation timescale of $t_{\text{relax}} \approx 2.8$ yr. These results highlight that there will not be significant deviations between the altimetry-based and inversion-based volume-change estimates over the current ICESat-2 time period if the ice viscosity reaches this magnitude. We provide an example of this behavior below. In all examples herein, we set the regularization parameter to $\varepsilon = 1$ in equation (19), which results in accurate reconstructions of the synthetic examples without overfitting the data.

Next, we show an example with synthetic data produced by a fully nonlinear model to test the assumptions underlying the small-perturbation approach (Stubblefield and others, 2021b, 2021a). The nonlinear model assumes a Glen's law viscosity (Glen, 1955; Cuffey and Paterson, 2010), a nonlinear Weertman-style sliding law (Weertman, 1957), fully nonlinear surface kinematic equations, and vanishing basal drag over the lake. For this example, we have assumed radial symmetry with respect to the map-plane coordinates (x, y) to facilitate numerical solution in three spatial dimensions. We also prescribe a more complex volume-change time series with a duration of three years in accordance with the current ICESat-2 time span and choose a lower viscosity for this example, $\bar{\eta} = 10^{14}$ Pa s (Fig. 4). Despite the simplifications inherent to the inverse method, the inversion accurately recovers the volume change time series that is produced by the nonlinear model (Fig. 4). Most importantly, the inversion is much more accurate than the surface-based volume change for this parameter regime. This example shows that ice viscosities on the order of $\bar{\eta} = 10^{14}$ Pa s can result in significant volume-change deviations over the current ICESat-2 time span. In particular, the examples in Figure 3 and Figure 4 show that the altimetry-based estimate tends to underestimate the magnitude of the true water volume change, regardless of whether the

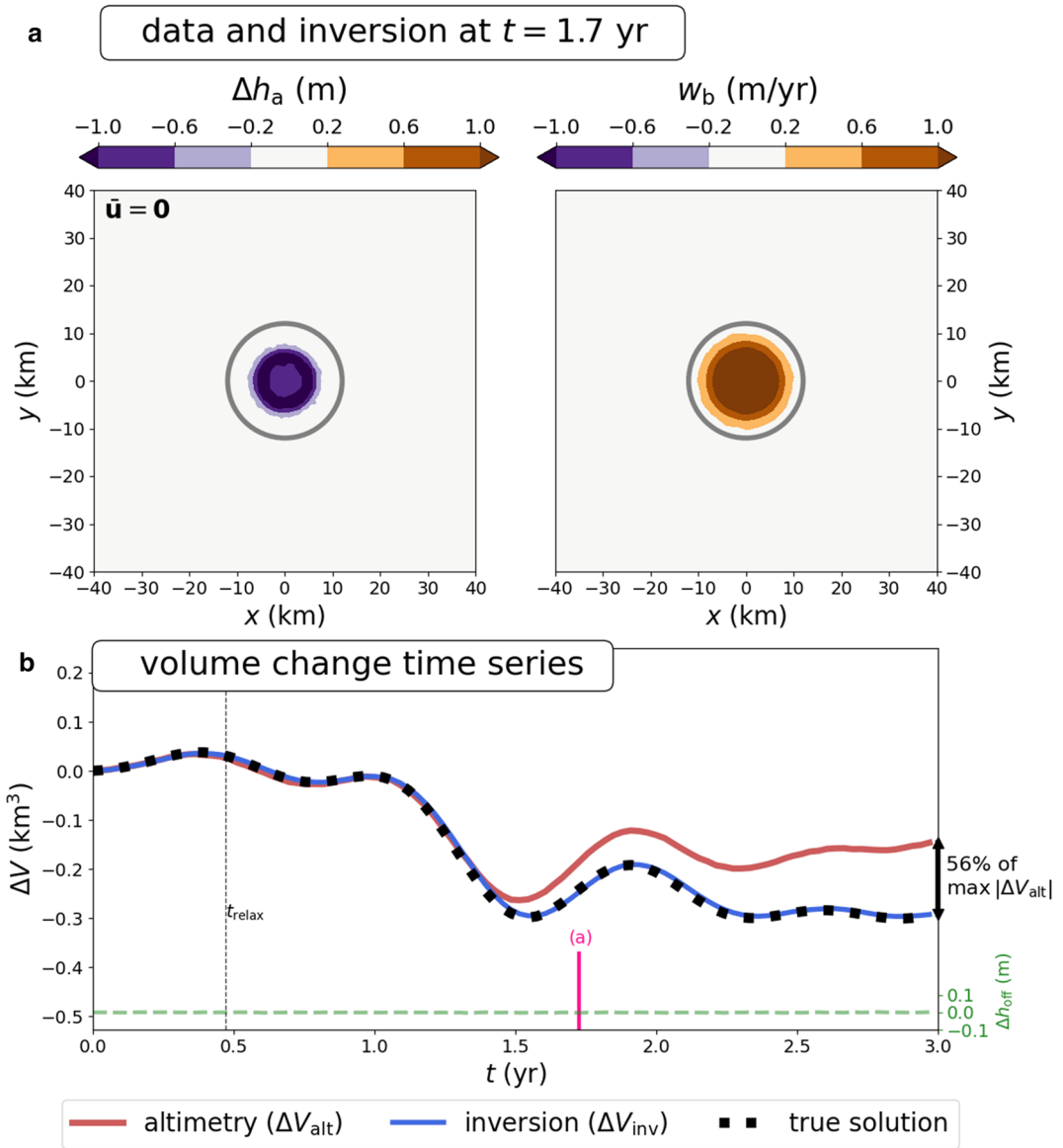


Figure 4. Inversion results for synthetic data produced with a radially-symmetric nonlinear Stokes model (Stubblefield and others, 2021b). (a) Map-plane elevation anomaly and inversion at $t = 1.7$ yr. (b) Time series of the surface-derived volume change (ΔV_{alt}), the inversion-based volume change (ΔV_{inv}), and the off-lake component (Δh_{off}) that is removed prior to inversion. The gray contours in (a) and (b) show the boundaries used to compute the volume-change time series. The maximum deviation between the surface-derived volume change and inversion in (b) is 0.15 km^3, or 56% of the maximum amplitude of the surface-derived estimate. The inversion accurately recovers the true water-volume change (dashed black line). The parameters for this example are $\bar{H} = 1500$ m, $\bar{\eta} = 10^{14}$ Pa s, $\bar{\beta} = 10^{10}$ Pa s m^{-1}, $\bar{u} = 0$ m yr^{-1}, and $\bar{v} = 0$ m yr^{-1}. The viscous relaxation time associated with these parameters is $t_{\text{relax}} = 0.47$ yr. The pink line marks the time step shown in (a). See Movie S2 for a detailed animation of the nonlinear model and Movie S3 for an animation of the inversion over all time steps.

https://doi.org/10.1017/jog.2023.90 Published online by Cambridge University Press

volume change is positive or negative. Next, we describe the data and preprocessing steps before discussing examples of ICESat-2 inversions.

4. Data and preprocessing

We use the ICESat-2 ATL15 L3B Gridded Antarctic and Arctic Land Ice Height Change (Version 2) data product (Smith and others, 2022) to obtain elevation-change anomalies above the Antarctic subglacial lakes shown in Figure 1. The map-plane $(x,\ y)$ coordinates in the ATL15 dataset correspond to the Antarctic Polar Stereographic Projection based on the WGS-84 ellipsoid (EPSG:3031). For the examples explored here, we interpolated the ICESat-2 ATL15 data onto a space-time grid with 100 points in each direction $(t,\ x,\ y)$ to obtain the same resolution as the numerical model. Alternatively, we could restrict the model-data misfit in (18) to the discrete set of data points, but this could require additional temporal regularization that we have not included in this study. We remove any regional thickening or thinning trends by subtracting the spatially averaged off-lake component, Δh_{off}, as described below. We also have to establish a reference elevation profile to define the elevation-change anomaly. By default, the elevation changes in ATL15 are relative to the ice-surface elevation on January 1, 2020. In general, the elevation anomaly can be defined relative to any of the ATL15 time points by subtracting the elevation surface at a particular reference time t_{ref}. Therefore, the elevation change anomaly is derived from the ATL15 elevation change product Δh via

$$\Delta h_{\text{a}}(x, y, t) = \Delta h(x, y, t) - \Delta h_{\text{off}}(t) - \left[\Delta h(x, y, t_{\text{ref}}) - \Delta h_{\text{off}}(t_{\text{ref}})\right] \tag{23}$$

where Δh_{off} is the (time-varying) spatial average of Δh away from the lake. Here, the spatial average is taken over all points that are at a distance greater than 80% from the centroid of the lake to the boundary of the computational domain.

Based on previously identified lake activity, an appropriate reference time t_{ref} to define the anomalies happens to be the initial time in the ATL15 product, October 1, 2018, for all of the lakes considered here except Mercer Subglacial Lake (SLM). SLM reached an apparent highstand near the end of 2017 before beginning a drainage event during the ICESat-2 period (Siegfried and Fricker, 2021), so the initial time in the ICESat-2 data does not correspond to an elevation anomaly of zero. We elaborate on this decision for each lake in more detail below and provide further commentary on preprocessing considerations in the discussion.

To invert the elevation-change data, we also must supply the approximate ice thickness $\bar{H}$, ice viscosity $\bar{\eta}$, basal drag coefficient $\bar{\beta}$, and horizontal ice velocity $\bar{\boldsymbol{u}} = [\bar{u},\ \bar{v}]^{\text{T}}$ that describe the reference ice-flow state (Fig. 2). The viscosity and basal drag estimates are derived from the inversions presented in Arthern and others (2015), which relied on the ALBMAP ice thickness (Le Brocq and others, 2010) and the MEaSUREs InSAR-Based Antarctic Ice Velocity Map (Version 1) (Rignot and others, 2011; Mouginot and others, 2012). However, we obtain horizontal surface velocity from the MEaSUREs Phase-Based Antarctic Ice Velocity Map (Version 1) (Mouginot and others, 2019a, 2019b) and ice thickness from MEaSUREs BedMachine Antarctica (Version 3) (Morlighem and others, 2020; Morlighem, 2022) for greater compatibility with the ICESat-2 epoch. All parameter values are obtained by calculating the mean of these data over the extent of the computational domain. The parameter values for each example are reported in Table 1 and the figure captions. To define the boundaries B in the volume estimation equations (21) and (22), we use the latest subglacial boundary inventory (Siegfried and Fricker, 2018), which is a compilation of static active subglacial lake outlines from a variety of sources that used mixed delineation methods.

5. ICESat-2 examples

Next, we will invert ICESat-2 data (ATL15 gridded elevation-change product) for the subglacial lakes shown in Figure 1: Lake Mac1 beneath the MacAyeal Ice Stream (e.g., Fricker and others, 2010; Siegfried and Fricker, 2018, 2021), Mercer Subglacial Lake at the confluence of Mercer Ice Stream and Whillans Ice Stream (e.g., Fricker and others, 2007; Siegfried and Fricker, 2018, 2021; Siegfried and others, 2023), Slessor_{23} beneath Slessor Glacier (Siegfried and Fricker, 2018; Siegfried and others, 2021), Thw_{170} beneath Thwaites Glacier (Smith and others, 2017; Hoffman and others, 2020) and Byrd_{s10} beneath Byrd Glacier in East Antarctica (Smith and others, 2009; Wright and others, 2014). These lakes have been the subject of numerous previous investigations and represent a wide range of filling-draining patterns, physical conditions, and locations across the Antarctic Ice Sheet (Table 1). For these examples, it is important to consider the reference time t_{ref} used to define the elevation anomaly in equation (23). We base our choices on the lake activity leading up to the ICESat-2 epoch. For example, subglacial lake Mac1 showed little activity since the beginning of the ICESat-2 epoch in 2018 (Siegfried and Fricker, 2021), suggesting that the initial time in the ATL15 data is an appropriate choice of reference time. For Mac1, there is a maximum discrepancy of ~0.12 km^3 between the surface-based and inversion-based volume-change estimates, or 24% of the maximum amplitude of the surface-derived estimate (Fig. 5).

We also show inversions of Mercer Subglacial Lake (SLM), which displays multiple oscillations over the ICESat-2 period (Fig. 6). We set the reference time to be $t = 1.3$ yr after the initial time (i.e. around the second peak in the time series), as this more closely corresponds to the long-term mean of Mercer Subglacial Lake's oscillation pattern (Siegfried and Fricker, 2021). For this example, we find a maximum discrepancy of ~0.05 km^3 between the surface-based and inversion-based volume-change estimates, or 19% of the maximum amplitude of the surface-derived estimate.

We also invert elevation anomalies from Slessor Glacier (lake Slessor_{23}) and Thwaites Glacier (lake Thw_{170}). Slessor_{23} shows a

Table 1. Parameters used in the inversions of the Antarctic subglacial lakes shown in Figure 1

Parameter	units	Mac1	SLM	Slessor_{23}	Thw_{170}	Byrd_{s10}
$\bar{H}$: ice thickness	m	926	1003	1735	2558	2676
$\bar{\eta}$: ice viscosity	Pa s ($\times 10^{14}$)	2.3	2.2	2.4	5.7	50.0
$\bar{\beta}$: basal drag coefficient	Pa s m^{-1} ($\times 10^{10}$)	7.4	37.0	2.7	1.3	14.0
$\bar{u}$: surface velocity (x)	m yr^{-1}	334	172	−141	−130	−9.4
$\bar{v}$: surface velocity (y)	m yr^{-1}	−178	−65	−146	−78	−9.8
lake centroid $(x,\ y)$	(km,km)	(−623, −899)	(−295, −501)	(−408, 1029)	(−1377, −395)	(583, −671)

Data sources are described in the "Data and Preprocessing" section. The velocity and centroid are listed in terms of the Antarctic Polar Stereographic Projection coordinates (EPSG:3031).

https://doi.org/10.1017/jog.2023.90 Published online by Cambridge University Press

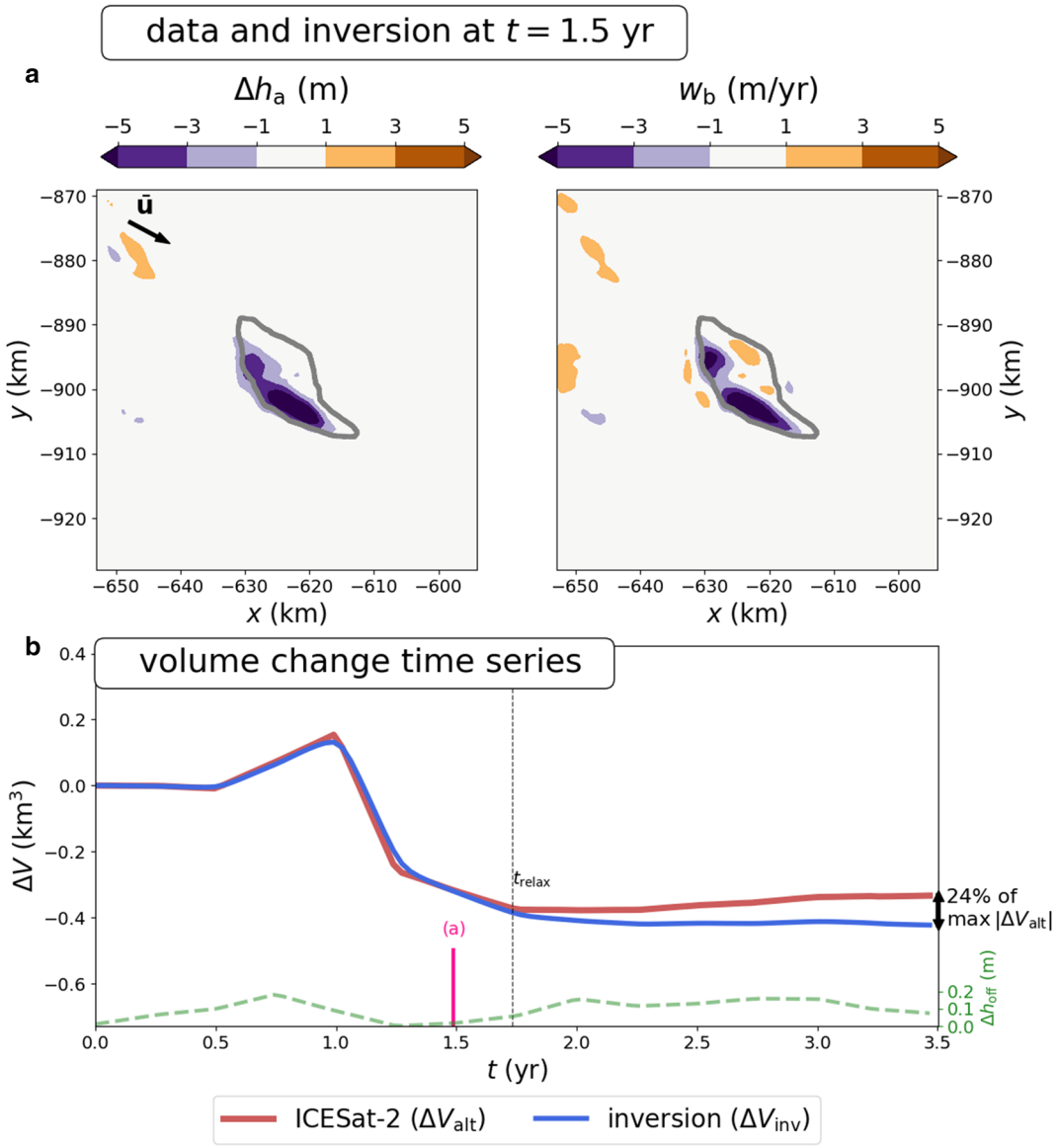


Figure 5. Inversion results for subglacial lake Mac1. (a) Map-plane elevation anomaly and inversion at $t = 1.5$ yr. (b) Time series of the surface-derived volume change (ΔV_{alt}), the inversion-based volume change (ΔV_{inv}), and the off-lake component (Δh_{off}) that is removed prior to inversion. The gray contours in (a) and (b) show the boundaries used to compute the volume-change time series (Siegfried and Fricker, 2018). The ice flow direction is shown by the black arrow in (a). The maximum deviation between the surface-derived volume change and inversion is 0.09 km^3, or 24% of the maximum amplitude of the surface-derived estimate. The parameters for this example are $\bar{H} = 926$ m, $\bar{\eta} = 2.3 \times 10^{14}$ Pa s, $\bar{\beta} = 7.4 \times 10^{10}$ Pa s m^{-1}, $\bar{u} = 334$ m yr^{-1}, and $\bar{v} = -178$ m yr^{-1}. The viscous relaxation time associated with these parameters is $t_{relax} = 1.73$ yr. The pink line marks the time step shown in (a). See Movie S4 for an animation of the inversion over all time steps.

discrepancy of ~0.52 km^3 between the volume-change estimates, which is 62% of the maximum amplitude of the surface-derived estimate (Fig. 7). Thw$_{170}$ also shows a large discrepancy of ~0.21 km^3, or 49% of the maximum in the altimetry-based estimate (Fig. 8). For Slessor$_{23}$, the initial time in the ICESat-2 data appears to be close to the midpoint of a filling stage, so this reference time seems appropriate for defining the elevation anomaly (Siegfried and Fricker, 2018). On the other hand, Thw$_{170}$ appears to be coming out of a quiescent post-drainage period at the beginning of the ICESat-2 period, so choosing the correct reference time is more ambiguous in this case (Hoffman and others, 2020; Malczyk and others, 2020). For example, setting the reference time to $t = 1.5$ yr instead results in a maximum discrepancy of ~0.075 km^3 between the volume-change estimates for the Thw$_{170}$ inversion. This discrepancy arises because the magnitude of the elevation-change anomaly is diminished when choosing the different reference time and less of the signal is attributed to the basal forcing. We quantify the sensitivity to the reference time more thoroughly in Appendix A and highlight the main issues in the discussion.

The common theme of the preceding examples is that they have ice viscosities on the order of $\bar{\eta} = 10^{14}$ Pa s (Table 1) and volume-change discrepancies that are at least ~ 20% of the maximum of the altimetry-based estimate (Figs. 5–8). The range of basal drag coefficients and ice thicknesses across these examples (Table 1) suggests that the ice viscosity is the primary parameter controlling the volume-change discrepancies. At higher viscosity values, the volume-change discrepancies diminish over the current ICESat-2 time period because the viscous relaxation time exceeds the oscillation timescale. To illustrate this behavior, we inverted ICESat-2 data over subglacial lake Byrd$_{s10}$ and found a much smaller discrepancy (~ 4%) between the surface-based and inversion-based volume estimates (Fig. 9). This lack of discrepancy arises because the ice over this lake has a viscosity of $\bar{\eta} = 5 \times 10^{15}$ Pa s, an order of magnitude higher than the preceding ICESat-2 examples. In this case, the surface and basal motion

https://doi.org/10.1017/jog.2023.90 Published online by Cambridge University Press

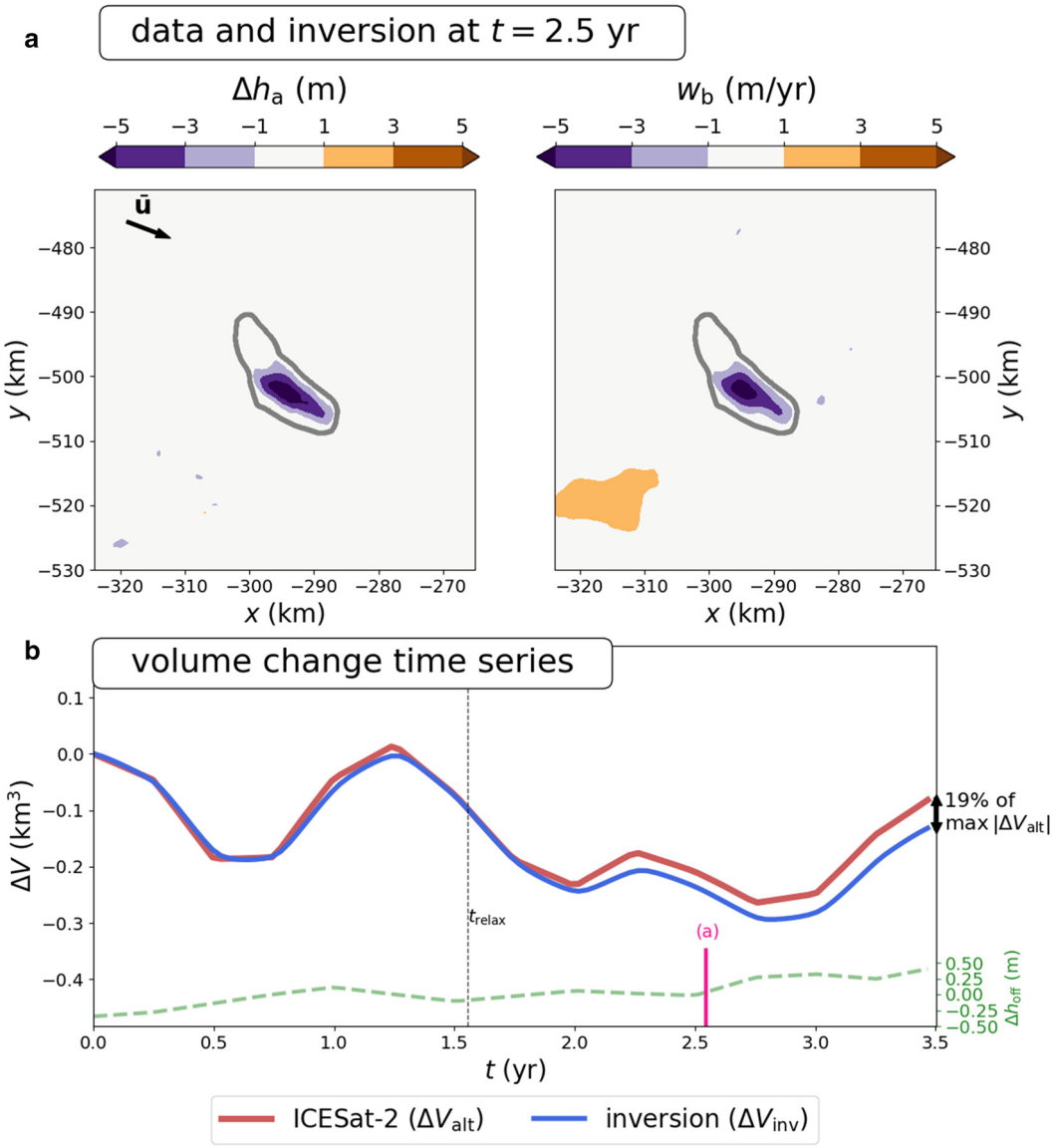


Figure 6. Inversion results for Mercer Subglacial Lake (SLM in Fig. 1). (a) Map-plane elevation anomaly and inversion at $t = 2.5$ yr. (b) Time series of the surface-derived volume change (ΔV_{alt}), the inversion-based volume change (ΔV_{inv}), and the off-lake component (Δh_{off}) that is removed prior to inversion. The gray contours in (a) and (b) show the boundaries used to compute the volume-change time series (Siegfried and Fricker, 2018). The ice flow direction is shown by the black arrow in (a). The maximum deviation between the surface-derived volume change and inversion in (b) is 0.05 km^3, or 19% of the maximum amplitude of the surface-derived estimate. The parameters for this example are $\bar{H} = 1003$ m, $\bar{\eta} = 2.2 \times 10^{14}$ Pa s, $\bar{\beta} = 3.7 \times 10^{11}$ Pa s m^{-1}, $\bar{u} = 172$ m yr^{-1}, and $\bar{v} = -65$ m yr^{-1}. The viscous relaxation time associated with these parameters is $t_{relax} = 1.56$ yr. The pink line marks the time step shown in (a). See Movie S5 for an animation of the inversion over all time steps.

correspond more closely because the viscous relaxation time, $t_{relax} = 13$ yr, is much longer than the current ICESat-2 time span. However, over decadal timescales larger discrepancies are still possible for this parameter regime (e.g., Fig. 3) unless the lake oscillation period is small compared to the relaxation time (Stubblefield and others, 2021a).

6. Discussion

Several practical and technical challenges are worth considering when applying the inverse method. From a practical viewpoint, the primary challenge is deriving the elevation anomaly from the altimetry data. For example, the inversion results may be sensitive to the details of how any regional thickening or thinning trends are separated from the lake-related elevation changes (Fricker and Scambos, 2009; Smith and others, 2009; Siegfried and Fricker, 2018, 2021). The reference elevation profile that is used to define the elevation anomaly from the data can also influence the inversion results, as we discussed in the case of subglacial lake Thw$_{170}$. Likewise, choosing an appropriate reference elevation profile may be difficult when the ice-sheet surface profile is heavily textured or the initial time in the data is during a volume-change event. In the latter case, we have relied on records of lake oscillations from previous satellite altimetry missions to choose appropriate reference times (Siegfried and Fricker, 2018, 2021). In Appendix A, we quantify the sensitivity of inversion results to the choice of reference time for the synthetic data (Fig. 10) and Thw$_{170}$ (Fig. 11). The results highlight the importance of carefully considering the reference time or elevation profile that is used to define the elevation-change anomaly (Appendix A). We leave further exploration of the sensitivity of inversion results to preprocessing steps for future work.

The primary technical limitations of the perturbation-based inverse method is that the associated forward models are inherently linear, posed on geometrically simple domains, and cannot deviate significantly from the specified reference state. Although

https://doi.org/10.1017/jog.2023.90 Published online by Cambridge University Press

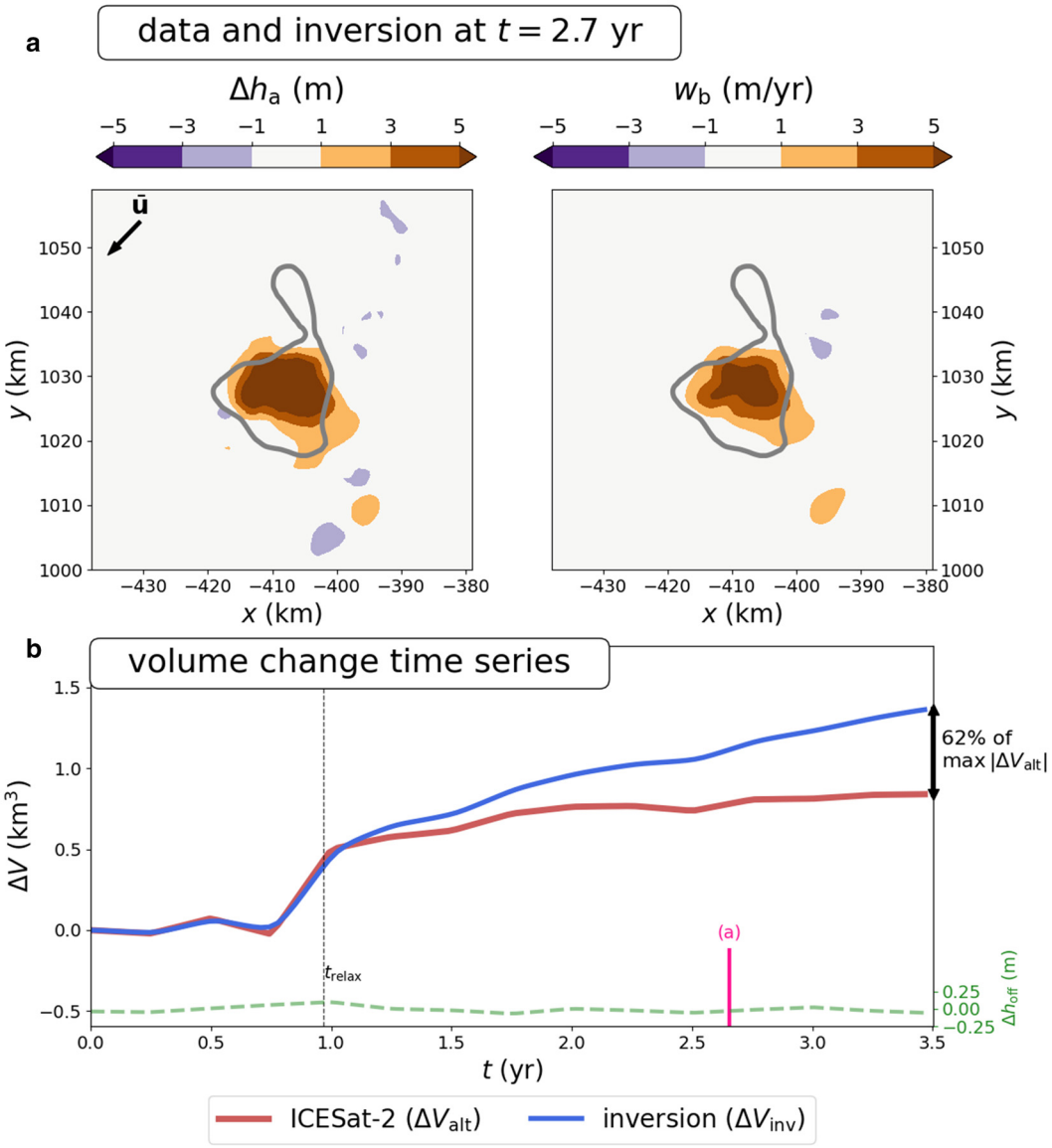


Figure 7. Inversion results for subglacial lake Slessor$_{23}$. (a) Map-plane elevation anomaly and inversion at $t = 2.7$ yr. (b) Time series of the surface-derived volume change (ΔV_{alt}), the inversion-based volume change (ΔV_{inv}), and the off-lake component (Δh_{off}) that is removed prior to inversion. The gray contours in (a) and (b) show the boundaries used to compute the volume-change time series (Siegfried and Fricker, 2018). The ice flow direction is shown by the black arrow in (a). The maximum deviation between the altimetry-derived volume change and inversion in (b) is 0.52 km^3, or 62% of the maximum amplitude of the surface-derived estimate. The parameters for this example are $\bar{H} = 1735$ m, $\bar{\eta} = 2.4 \times 10^{14}$ Pa s, $\bar{\beta} = 2.7 \times 10^{10}$ Pa s m^{-1}, $\bar{u} = -141$ m yr^{-1}, and $\bar{v} = -146$ m yr^{-1}. The viscous relaxation time associated with these parameters is $t_{relax} = 0.97$ yr. The pink line marks the time step shown in (a). See Movie S6 for an animation of the inversion over all time steps.

we have tested the validity of the method by inverting synthetic data from a simple radially symmetric nonlinear problem (Fig. 4), more complex problems could require alternative methods. For example, we would caution against applying the method to complex stress regimes like an ice-stream shear margin, which is the case for Engelhardt Subglacial Lake that lies beneath the margin of the Whillans Ice Stream (Fricker and others, 2007; Siegfried and others, 2016). We have also neglected any elastic components of ice deformation by assuming that ice flows as a viscous fluid because the filling-draining events considered herein span multiple years. However, elastic deformation can arise on shorter timescales near grounding lines when lake activity is related to tidal cycles (Milillo and others, 2017). Subglacial lakes have also been observed to drain on sub-weekly timescales during jökulhlaups in Iceland (Björnsson, 2002; Evatt and Fowler, 2007). Moreover, we have assumed that all of the elevation anomaly is driven by ice deformation rather than surface mass balance anomalies, which could arise, for example, from snow infilling the lake depression (Malczyk and others, 2020).

We have also assumed that, to first order, the subglacial lakes do not coincide with reductions in basal drag because the characteristic dipolar elevation anomaly associated with such slippery spots is not discernible in the examples considered herein (e.g., Gudmundsson, 2003; Sergienko and others, 2007). However, some large, inactive Antarctic subglacial lakes are known to coincide with slippery spots where the ice surface is flat over most of the lake except on the upstream side where thinning occurs and the downstream side where thickening occurs (Bell and others, 2006, 2007; Wright and Siegert, 2012). On the other hand, several West Antarctic ice streams also have both subglacial lakes and localized regions of anomalously high basal drag (sticky spots) in close proximity (Winberry and others, 2009; Sergienko and Hulbe, 2011; Winberry and others, 2014; Siegfried and others, 2016). This coupling can arise when enhanced basal traction

https://doi.org/10.1017/jog.2023.90 Published online by Cambridge University Press

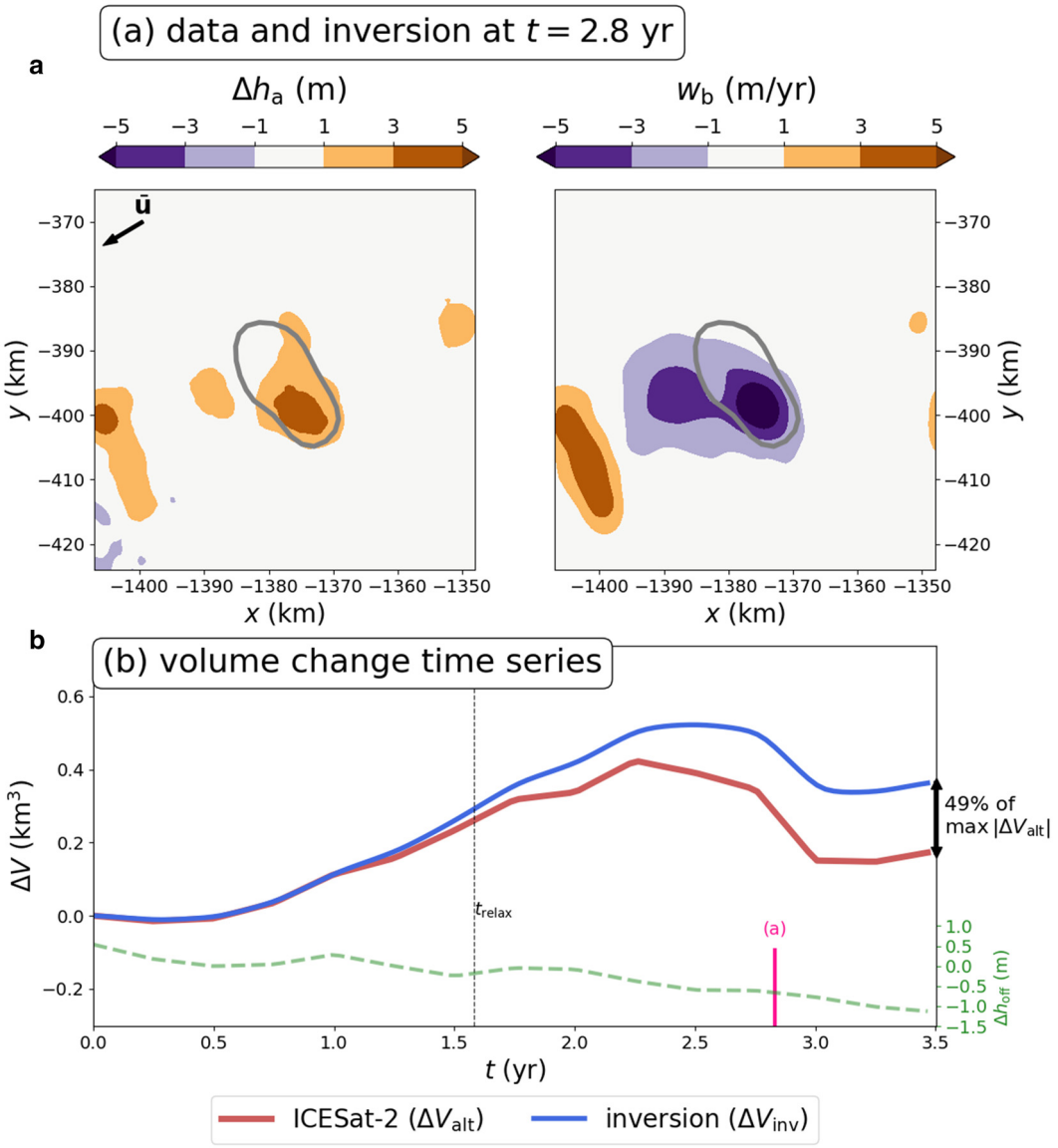


Figure 8. Inversion results for subglacial lake Thw_{170}. (a) Map-plane elevation anomaly and inversion at $t = 2.8$ yr. (b) Time series of the surface-derived volume change (ΔV_{alt}), the inversion-based volume change (ΔV_{inv}), and the off-lake component (Δh_{off}) that is removed prior to inversion. The gray contours in (a) and (b) show the boundaries used to compute the volume-change time series (Smith and others, 2017). The ice flow direction is shown by the black arrow in (a). The maximum deviation between the altimetry-derived volume change and inversion is 0.21 km^3, or 49% of the maximum amplitude of the surface-derived estimate. The parameters for this example are $\bar{H} = 2558$ m, $\bar{\eta} = 5.7 \times 10^{14}$ Pa s, $\bar{\beta} = 1.3 \times 10^{10}$ Pa s m^{-1}, $\bar{u} = -130$ m yr^{-1}, and $\bar{v} = -78$ m yr^{-1}. The viscous relaxation time associated with these parameters is $t_{relax} = 1.58$ yr. The pink line marks the time step shown in (a). See Movie S7 for an animation of the inversion over all time steps.

provides a meltwater source for the lakes or when lake drainage causes channelization that removes water from surrounding regions of the bed (Sergienko and Hulbe, 2011). Joint inversion for basal drag variations and lake activity would help to further refine our understanding of these coupled systems and may be tractable if an additional data source like surface velocity is available.

In this study, we have focused primarily on estimating subglacial water-volume changes. Another application of the inverse method will be estimating subglacial lake shorelines or areal extent. Lake boundaries are currently defined using ice-surface deformation extent to generate static lake boundaries (Siegfried and Fricker, 2018); however, these static boundaries were typically generated using lower spatial resolution altimetry instruments than are available today. This static view of lake boundaries has resulted in a number of lake re-delineation attempts (e.g., Fricker and others, 2014; Siegfried and Fricker, 2018) and more recent suggestions of time-variable lake boundaries (e.g., Neckel and others, 2021; Siegfried and Fricker, 2021). In our study, it is clear that static subglacial lake boundaries do not dependably encompass the ICESat-2 surface height change observations (Figs. 5–9) likely because lake shorelines vary temporally. Additionally, recent numerical modeling shows the surface-derived boundaries can have a larger areal extent than the true lake boundary at the base (Stubblefield and others, 2021a). With our inverse method, we could attempt to reconstruct subglacial shoreline evolution by tracking the areal extent of the basal forcing rather than the surface deformation. Improving the accuracy of subglacial-lake shoreline estimates in this way could be valuable for site selection in future subglacial drilling projects (Tulaczyk and others, 2014; Priscu and others, 2021) and thereby provide stronger constraints on subglacial microbial and geochemical processes (Christner and others, 2014; Achberger and others, 2016; Davis and others, 2023).

The inverse method could be extended to estimate other subglacial hydrological quantities besides water-volume changes. For

https://doi.org/10.1017/jog.2023.90 Published online by Cambridge University Press

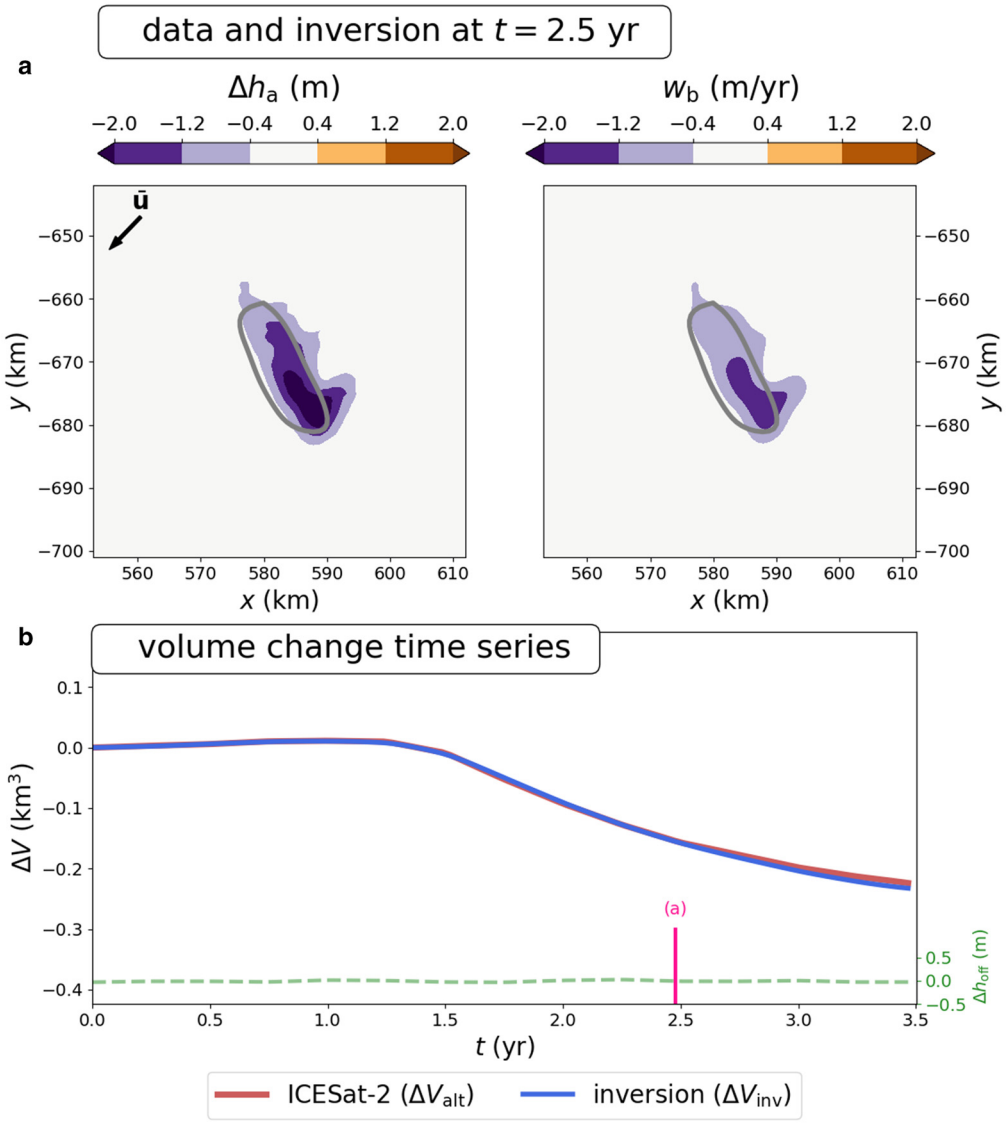


Figure 9. Inversion results for subglacial lake $Byrd_{s10}$. (a) Map-plane elevation anomaly and inversion at $t = 2.5$ yr. (b) Time series of the surface-derived volume change (ΔV_{alt}), the inversion-based volume change (ΔV_{inv}), and the off-lake component (Δh_{off}) that is removed prior to inversion. The gray contours in (a) and (b) show the boundaries used to compute the volume-change time series. The ice flow direction is shown by the black arrow in (a). The maximum deviation between the altimetry-derived volume change and inversion is 9×10^{-3} km^3, or 4% of the maximum amplitude of the surface-derived estimate. The parameters for this example are $\bar{H} = 2676$ m, $\bar{\eta} = 5 \times 10^{15}$ Pa s, $\bar{\beta} = 1.4 \times 10^{11}$ Pa s m^{-1}, $\bar{u} = -9.4$ m yr^{-1}, and $\bar{v} = -9.8$ m yr^{-1}. The viscous relaxation time associated with these parameters is $t_{relax} = 13$ yr. The pink line marks the time step shown in (a). See Movie S8 for an animation of the inversion over all time steps.

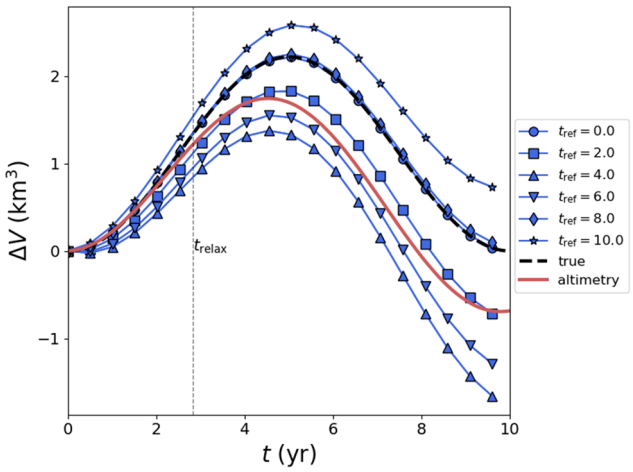


Figure 10. Inversion of synthetic data from Figure 3 after redefining the reference time t_{ref} in equation (23) to a range of incorrect values. The correct reference time in this example is $t_{ref} = 0$. Significant deviations between the inversion and true solution can occur if an incorrect reference time is chosen.

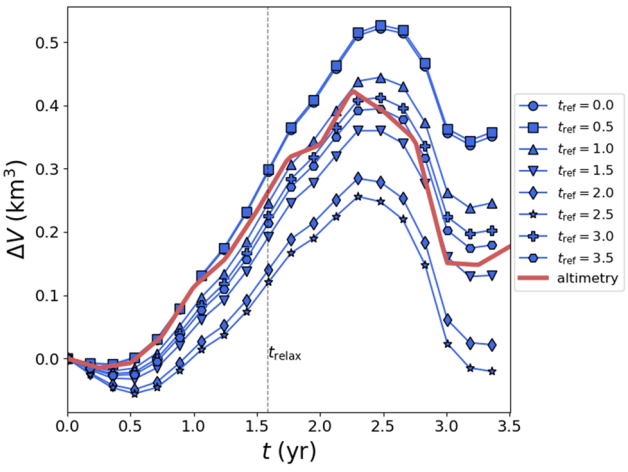


Figure 11. Inversion of the Thw_{170} data from Figure 8 after redefining the reference time t_{ref} in equation (23) to a range of alternative values.

https://doi.org/10.1017/jog.2023.90 Published online by Cambridge University Press

example, the temporal derivative of the volume change can be related to the relative volumetric water discharge into (or out of) the lake (Evatt and Fowler, 2007). The water discharge naturally appears in models of glacial lakes that are coupled to subglacial channel evolution (Fowler, 1999, 2009; Kingslake, 2015; Carter and others, 2017; Stubblefield and others, 2019; Jenson and others, 2022). Finally, an alternative to prescribing a basal vertical velocity anomaly would have been prescribing a basal pressure anomaly. In particular, converting between vertical velocity and pressure perturbations is straightforward with the spectral method employed here (e.g., Gudmundsson, 2003, equation 54). Pressure perturbations could possibly be related to the subglacial effective pressure, the difference between the cryostatic pressure and water pressure in the lake, since we have assumed that the pressure in the reference state is cryostatic (cf. Evatt and Fowler, 2007; Stubblefield and others, 2021b). Estimating the effective pressure or other hydrological quantities with altimetry would be valuable for further constraining the physics of subglacial drainage systems.

7. Conclusions

We have introduced and applied an inverse method for estimating the basal forcing associated with subglacial lake activity from ice-sheet altimetry. We have provided some validation of the small-perturbation approach by inverting synthetic data from a nonlinear subglacial lake model to obtain a basal vertical velocity field and water-volume change time series that agree with the nonlinear model. We then applied the method to a collection of Antarctic subglacial lakes by inverting satellite altimetry data from NASA's ICESat-2 mission. These results illustrate that there can be significant discrepancies between surface-based estimation methods and the inversion due to the effects of viscous ice flow. In particular, the results show that surface-based estimation methods can underestimate changes in subglacial water volume. The inverse method provides a simple way to refine basal water budget contributions derived from active subglacial lakes and further illuminate the physics of subglacial hydrological systems with satellite altimetry.

Supplementary material. The supplementary material for this article can be found at https://doi.org/10.1017/jog.2023.90

Data. All data used in this study are openly available:
ICESat-2 ATL15, Version 2 (https://doi.org/10.5067/ATLAS/ATL15.002),
WAVI ice-sheet model output (https://doi.org/10.5285/5F0AC285-CCA3-4A0E-BCBC-D921734395AB),
MEaSUREs Phase-Based Antarctica Ice Velocity Map, Version 1 (https://doi.org/10.5067/PZ3NJ5RXRH10),
MEaSUREs BedMachine Antarctica, Version 3 (https://doi.org/10.5067/FPSU0V1MWUB6),
Subglacial lake inventory from Siegfried and Fricker (2018) (https://doi.org/10.5281/zenodo.4914107). The code used to produce the results is openly available (https://doi.org/10.5281/zenodo.8371416).

Acknowledgements. Aaron Stubblefield thanks Jonathan Kingslake, Meredith Nettles, Ian Hewitt, and Brent Minchew for discussions about the inverse problem. Aaron Stubblefield was supported by NSF (2012958). Colin Meyer was supported by NSF (2012958); ARO (78811EG); and NASA (80NSSC21M0329). Matthew Siegfried and Wilson Sauthoff were supported by NASA (80NSSC21K0912).

References

Achberger AM and 35 others (2016) Microbial community structure of subglacial Lake Whillans, West Antarctica. *Frontiers in Microbiology* **7**(SEP), 1–13. doi:10.3389/fmicb.2016.01457

Arthern RJ, Hindmarsh RC and Williams CR (2015) Flow speed within the Antarctic ice sheet and its controls inferred from satellite observations. *Journal of Geophysical Research: Earth Surface* **120**(7), 1171–1188. doi:10.1002/2014JF003239

Atkinson K and Han W (2009) *Theoretical numerical analysis*. Vol. **39**. 3rd Edn, New York, NY: Springer.

Balise MJ and Raymond CF (1985) Transfer of basal sliding variations to the surface of a linearly viscous glacier. *Journal of Glaciology* **31**(109), 308–318. doi:10.3189/S002214300000664X

Bell RE, Studinger M, Fahnestock MA and Shuman CA (2006) Tectonically controlled subglacial lakes on the flanks of the Gamburtsev Subglacial Mountains, East Antarctica. *Geophysical Research Letters* **33**(2), L02504. doi:10.1029/2005GL025207

Bell RE, Studinger M, Shuman CA, Fahnestock MA and Joughin I (2007) Large subglacial lakes in East Antarctica at the onset of fast-flowing ice streams. *Nature* **445**(7130), 904–907. doi:10.1038/nature05554

Björnsson H (2002) Subglacial lakes and jökulhlaups in Iceland. *Global and Planetary Change* **35**(3–4), 255–271. doi:10.1016/S0921-8181(02)00130-3

Bowling J, Livingstone S, Sole A and Chu W (2019) Distribution and dynamics of Greenland subglacial lakes. *Nature Communications* **10**(1), 1–11. doi:10.1038/s41467-019-10821-w

Budd W (1970) Ice flow over bedrock perturbations. *Journal of Glaciology* **9**(55), 29–48. doi:10.3189/S0022143000026770

Carter SP, Fricker HA and Siegfried MR (2017) Antarctic subglacial lakes drain through sediment-floored canals: Theory and model testing on real and idealized domains. *Cryosphere* **11**(1), 381–405. doi:10.5194/tc-11-381-2017

Christner BC and 9 others (2014) A microbial ecosystem beneath the West Antarctic ice sheet. *Nature* **512**(7514), 310–313. doi:10.1038/nature13667

Cuffey KM and Paterson WSB (2010) *The Physics of Glaciers*. Amsterdam: Academic Press.

Davis CL and 9 others (2023) Biogeochemical and historical drivers of microbial community composition and structure in sediments from Mercer Subglacial Lake, West Antarctica. *ISME Communications* **3**(1), 8. doi:10.1038/s43705-023-00216-w

Evatt GW and Fowler AC (2007) Cauldron subsidence and subglacial floods. *Annals of Glaciology* **45**, 163–168. doi:10.3189/172756407782282561

Fowler A (1999) Breaking the seal at Grímsvötn, Iceland. *Journal of Glaciology* **45**(151), 506–516. doi:10.3189/S0022143000001362

Fowler A (2009) Dynamics of subglacial floods. *Proceedings of the Royal Society A: Mathematical, Physical and Engineering Sciences* **465**(2106), 1809–1828. doi:10.1098/rspa.2008.0488

Fricker HA and Scambos T (2009) Connected subglacial lake activity on lower Mercer and Whillans Ice Streams, West Antarctica, 2003-2008. *Journal of Glaciology* **55**(190), 303–315. doi:10.3189/002214309788608813

Fricker HA, Scambos T, Bindschadler R and Padman L (2007) An active subglacial water system in West Antarctica mapped from space. *Science* **315**(5818), 1544–1548. doi:10.1126/science.1136897

Fricker HA and 5 others (2010) Synthesizing multiple remote-sensing techniques for subglacial hydrologic mapping: application to a lake system beneath MacAyeal Ice Stream, West Antarctica. *Journal of Glaciology* **56**(196), 187–199. doi:10.3189/002214310791968557

Fricker HA, Carter SP, Bell RE and Scambos T (2014) Active lakes of Recovery Ice Stream, East Antarctica : a bedrock-controlled subglacial hydrological system. *Journal of Glaciology* **60**(223), 1015–1030. doi:10.3189/2014JoG14J063

Fricker HA, Siegfried MR, Carter SP and Scambos TA (2016) A decade of progress in observing and modeling Antarctic subglacial water systems. *Philosophical Transactions of the Royal Society A: Mathematical, Physical and Engineering Sciences* **374**(2059), 20140294. doi: 10.1098/rsta.2014.0294

Glen JW (1955) The creep of polycrystalline ice. *Proceedings of the Royal Society of London. Series A. Mathematical and Physical Sciences* **228**(1175), 519–538. doi:10.1098/rspa.1955.0066

Goldberg D, Heimbach P, Joughin I and Smith B (2015) Committed retreat of Smith, Pope, and Kohler Glaciers over the next 30 years inferred by transient model calibration. *The Cryosphere* **9**(6), 2429–2446. doi:10.5194/tc-9-2429-2015

Gray L and 5 others (2005) Evidence for subglacial water transport in the West Antarctic Ice Sheet through three-dimensional satellite radar interferometry. *Geophysical Research Letters* **32**(3), L03501. doi:10.1029/2004GL021387

Greve R and Blatter H (2009) *Dynamics of ice sheets and glaciers*. Berlin: Springer Science & Business Media.

Gudmundsson GH (2003) Transmission of basal variability to a glacier surface. *Journal of Geophysical Research: Solid Earth* **108**(B5), 2253. doi:10.1029/2002JB002107

Gudmundsson GH and Raymond M (2008) On the limit to resolution and information on basal properties obtainable from surface data on ice streams. *The Cryosphere* **2**(2), 167–178. doi:10.5194/tc-2-167-2008

Hanke M (2017) *A Taste of Inverse Problems: Basic Theory and Examples*. Philadelphia, PA.: SIAM.

Hoffman AO, Christianson K, Shapero D, Smith BE and Joughin I (2020) Brief communication: Heterogenous thinning and subglacial lake activity on Thwaites Glacier, West Antarctica. *The Cryosphere* **14**(12), 4603–4609. doi:10.5194/tc-14-4603-2020

Hutter K, Legerer F and Spring U (1981) First-order stresses and deformations in glaciers and ice sheets. *Journal of Glaciology* **27**(96), 227–270. doi:10.3189/S0022143000015379

Jenson A, Amundson JM, Kingslake J and Hood E (2022) Long-period variability in ice-dammed glacier outburst floods due to evolving catchment geometry. *The Cryosphere* **16**(1), 333–347. doi:10.5194/tc-16-333-2022

Kingslake J (2015) Chaotic dynamics of a glaciohydraulic model. *Journal of Glaciology* **61**(227), 493–502. doi:10.3189/2015JoG14J208

Larour E and 8 others (2014) Inferred basal friction and surface mass balance of the Northeast Greenland Ice Stream using data assimilation of ICESat (Ice Cloud and land Elevation Satellite) surface altimetry and ISSM (Ice Sheet System Model). *The Cryosphere* **8**(6), 2335–2351. doi:10.5194/tc-8-2335-2014

Le Brocq AM, Payne AJ and Vieli A (2010) An improved Antarctic dataset for high resolution numerical ice sheet models (ALBMAP v1). *Earth System Science Data* **2**(2), 247–260. doi:10.5194/essd-2-247-2010

Livingstone SJ and 5 others (2019) Brief communication: Subglacial lake drainage beneath Isunguata Sermia, West Greenland: Geomorphic and ice dynamic effects. *The Cryosphere* **13**(10), 2789–2796. doi:10.5194/tc-13-2789-2019

Livingstone SJ and 9 others (2022) Subglacial lakes and their changing role in a warming climate. *Nature Reviews Earth & Environment* **3**(2), 106–124. doi:10.1038/s43017-022-00262-3

Malczyk G, Gourmelen N, Goldberg D, Wuite J and Nagler T (2020) Repeat subglacial lake drainage and filling beneath Thwaites Glacier. *Geophysical Research Letters* **47**(23), e2020GL089658. doi:10.1029/2020GL089658

Markus T and 9 others (2017) The Ice, Cloud, and land Elevation Satellite-2 (ICESat-2): science requirements, concept, and implementation. *Remote Sensing of Environment* **190**, 260–273. doi:10.1016/j.rse.2016.12.029

Milillo P and 6 others (2017) On the short-term grounding zone dynamics of Pine Island Glacier, West Antarctica, observed with COSMO-SkyMed interferometric data. *Geophysical Research Letters* **44**(20), 10436–10444. doi:10.1002/2017GL074320

Morlighem M (2022) MEaSUREs BedMachine Antarctica, Version 3.

Morlighem M and 9 others (2020) Deep glacial troughs and stabilizing ridges unveiled beneath the margins of the Antarctic ice sheet. *Nature Geoscience* **13**(2), 132–137. doi:10.1038/s41561-019-0510-8

Mosbeux C, Gillet-Chaulet F and Gagliardini O (2016) Comparison of adjoint and nudging methods to initialise ice sheet model basal conditions. *Geoscientific Model Development* **9**(7), 2549–2562. doi:10.5194/gmd-9-2549-2016

Mouginot J, Scheuchl B and Rignot E (2012) Mapping of ice motion in Antarctica using synthetic-aperture radar data. *Remote Sensing* **4**(9), 2753–2767. doi:10.3390/rs4092753

Mouginot J, Rignot E and Scheuchl B (2019a) MEaSUREs Phase-Based Antarctica Ice Velocity Map, Version 1.

Mouginot J, Rignot E and Scheuchl B (2019b) Continent-wide, interferometric SAR phase, mapping of Antarctic ice velocity. *Geophysical Research Letters* **46**(16), 9710–9718. doi:10.1029/2019GL083826

Neckel N, Franke S, Helm V, Drews R and Jansen D (2021) Evidence of cascading subglacial water flow at Jutulstraumen Glacier (Antarctica) derived from Sentinel-1 and ICESat-2 measurements. *Geophysical Research Letters* **48**(20), e2021GL094472. doi:10.1029/2021GL094472

Priscu JC and 9 others (2021) Scientific access into Mercer Subglacial Lake: scientific objectives, drilling operations and initial observations. *Annals of Glaciology* **62**(85-86), 340–352. doi:10.1017/aog.2021.10

Rignot E, Mouginot J and Scheuchl B (2011) Ice flow of the Antarctic ice sheet. *Science* **333**(6048), 1427–1430. doi:10.1126/science.1208336

Scambos TA, Berthier E and Shuman CA (2011) The triggering of subglacial lake drainage during rapid glacier drawdown: Crane Glacier, Antarctic Peninsula. *Annals of Glaciology* **52**(59), 74–82. doi:10.3189/172756411799096204

Sergienko O (2012) The effects of transverse bed topography variations in ice-flow models. *Journal of Geophysical Research: Earth Surface* **117**(F3), F03011. doi:10.1029/2011JF002203

Sergienko OV and Hulbe CL (2011) 'Sticky spots' and subglacial lakes under ice streams of the Siple Coast, Antarctica. *Annals of Glaciology* **52**(58), 18–22. doi:10.3189/172756411797252176

Sergienko OV, MacAyeal DR and Bindschadler RA (2007) Causes of sudden, short-term changes in ice-stream surface elevation. *Geophysical Research Letters* **34**(22), L22503. doi:10.1029/2007GL031775

Siegfried M and Fricker H (2021) Illuminating active subglacial lake processes with ICESat-2 laser altimetry. *Geophysical Research Letters* **48**(14), e2020GL091089. doi:10.1029/2020GL091089

Siegfried M and 22 others (2023) The life and death of a subglacial lake in West Antarctica. *Geology* **51**(5), 434–438. doi:10.1130/G50995.1

Siegfried MR, Fricker HA, Carter SP and Tulaczyk S (2016) Episodic ice velocity fluctuations triggered by a subglacial flood in West Antarctica. *Geophysical Research Letters* **43**(6), 2640–2648. doi:10.1002/2016GL067758

Siegfried MR and Fricker HA (2018) Thirteen years of subglacial lake activity in Antarctica from multi-mission satellite altimetry. *Annals of Glaciology* **59**, 1–14. doi:10.1017/aog.2017.36

Siegfried MR, Schroeder DM, Sauthoff W and Smith B (2021) Investigating a large subglacial lake drainage in East Antarctica with ice-penetrating radar. In *SEG/AAPG/SEPM First International Meeting for Applied Geoscience & Energy*, OnePetro.

Smith B and 13 others (2022) ATLAS/ICESat-2 L3B Gridded Antarctic and Arctic Land Ice Height Change, Version 2.

Smith BE, Fricker HA, Joughin IR and Tulaczyk S (2009) An inventory of active subglacial lakes in Antarctica detected by ICESat (2003–2008). *Journal of Glaciology* **55**(192), 573–595. doi:10.3189/002214309789470879

Smith BE, Gourmelen N, Huth A and Joughin I (2017) Connected subglacial lake drainage beneath Thwaites Glacier, West Antarctica. *Cryosphere* **11**(1), 451–467. doi:10.5194/tc-11-451-2017

Stadler G (2009) Elliptic optimal control problems with L1-control cost and applications for the placement of control devices. *Computational Optimization and Applications* **44**(2), 159. doi:10.1007/s10589-007-9150-9

Stearns LA, Smith BE and Hamilton GS (2008) Increased flow speed on a large east Antarctic outlet glacier caused by subglacial floods. *Nature Geoscience* **1**(12), 827–831. doi:10.1038/ngeo356

Stubblefield AG (2022) *Modelling the dynamics and surface expressions of subglacial water flow*. Ph.D. thesis, Columbia University.

Stubblefield AG, Creyts TT, Kingslake J and Spiegelman M (2019) Modeling oscillations in connected glacial lakes. *Journal of Glaciology* **65**(253), 745–758. doi:10.1017/jog.2019.46

Stubblefield AG, Creyts TT, Kingslake J, Siegfried MR and Spiegelman M (2021a) Surface expression and apparent timing of subglacial lake oscillations controlled by Viscous ice flow. *Geophysical Research Letters* **48**(17), e2021GL094658. doi:10.1029/2021GL094658

Stubblefield AG, Spiegelman M and Creyts TT (2021b) Variational formulation of marine ice-sheet and subglacial-lake grounding-line dynamics. *Journal of Fluid Mechanics* **919**, A23. doi:10.1017/jfm.2021.394

Thorsteinsson T and 5 others (2003) Bed topography and lubrication inferred from surface measurements on fast-flowing ice streams. *Journal of Glaciology* **49**(167), 481–490. doi:10.3189/172756503781830502

Tulaczyk S and 16 others (2014) WISSARD at subglacial Lake Whillans, West Antarctica: scientific operations and initial observations. *Annals of Glaciology* **55**(65), 51–58. doi:10.3189/2014AoG65A009

Turcotte DL and Schubert G (2014) *Geodynamics*. 3rd Edn, Cambridge: Cambridge University Press.

Virtanen P and 34 others (2020) SciPy 1.0: fundamental algorithms for scientific computing in Python. *Nature Methods* **17**, 261–272. doi:10.1038/s41592-019-0686-2

Vogel CR (2002) *Computational Methods for Inverse Problems*. Society for Industrial and Applied Mathematics.

Weertman J (1957) On the sliding of glaciers. *Journal of Glaciology* **3**(21), 33–38. doi:10.3189/S0022143000024709

Winberry JP, Anandakrishnan S and Alley RB (2009) Seismic observations of transient subglacial water-flow beneath MacAyeal Ice Stream, West Antarctica. *Geophysical Research Letters* **36**(11), L11502. doi:10.1029/2009GL037730

Winberry JP, Anandakrishnan S, Alley RB, Wiens DA and Pratt MJ (2014) Tidal pacing, skipped slips and the slowdown of Whillans Ice Stream, Antarctica. *Journal of Glaciology* **60**(222), 795–807. doi:10.3189/2014JoG14J038

Wingham DJ, Siegert MJ, Shepherd A and Muir AS (2006) Rapid discharge connects Antarctic subglacial lakes. *Nature* **440**(7087), 1033–1036. doi:10.1038/nature04660

https://doi.org/10.1017/jog.2023.90 Published online by Cambridge University Press

Wright A and Siegert M (2012) A fourth inventory of Antarctic subglacial lakes. *Antarctic Science* **24**(6), 659–664. doi:10.1017/S095410201200048X

Wright A and 6 others (2014) Subglacial hydrological connectivity within the Byrd Glacier catchment, East Antarctica. *Journal of Glaciology* **60**(220), 345–352. doi:10.3189/2014jog13j014

APPENDIX A. Sensitivity to reference time

As noted in the results and discussion, the primary challenge of applying the inverse method in practice is defining the elevation-change anomaly from the data. We must choose a reference time t_{ref} to define the anomaly through equation (23). To explore this sensitivity further, we inverted the synthetic data (Fig. 3) after re-defining the anomaly to be zero at a range of incorrect reference times. The results show that choosing an appropriate reference time has a strong influence on the validity of the inversion. Choosing an incorrect reference time can cause significant deviations between the inversion and the true solution (Fig. 10).

We repeated the experiment by inverting the Thw_{170} data after re-defining the anomaly to be zero at a range of alternative reference times (Fig. 11). We find that none of the options correspond exactly to the altimetry-based estimate over the ICESat-2 time period, although the earlier reference times ($t_{\text{ref}} \leq 1$) correspond more closely to the expected behavior of a lake undergoing a filling stage (e.g., Fig. 3). Even so, it not entirely clear based on previously published data which option is the most valid (Hoffman and others, 2020). Further investigation to determine when local perturbations in glacier surface elevation reach a viscously relaxed state in more complex settings (e.g., Thwaites Glacier) would be valuable.

https://doi.org/10.1017/jog.2023.90 Published online by Cambridge University Press